Engineering Fracture Mechanics 253 (2021) 107876

Contents lists available at ScienceDirect

Engineering Fracture Mechanics

journal homepage: www.elsevier.com/locate/engfracmech

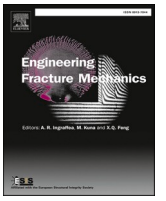

Characterising and representing small crack growth in an additive manufactured titanium alloy

Muhammad Shamir, Xiang Zhang *, Abdul Khadar Syed

Faculty of Engineering, Environment and Computing, Coventry University, Coventry CV1 5FB, UK

ARTICLE INFO

Keywords:
Small/short cracks
EIDS
Surface roughness
Durability
Fracture mechanics
Finite element analysis
WAAM
Ti-6Al-4V

ABSTRACT

The purpose of the research is to apply the modified Hartman-Schijve equation for predicting small crack growth rate in an additive manufactured titanium Ti-6Al-4V. Material constants in the equation were determined by long crack test data, and the threshold value of the stress intensity factor range was set to a small value. A small fatigue crack test was conducted to validate the fitted equation. Predicted fatigue life of another specimen configuration under bending load agreed well with the test result. The work shows that it may be possible to represent both small and long crack growth rates by the modified Hartman-Schijve equation with its material constants being determined by long crack test.

1. Introduction

Additive manufacturing (AM) of titanium Ti-6Al-4V (Ti64) has received particular attention in research and development in the aerospace, energy, and biomedical industries owing to its high strength-to-weight ratio, high fracture toughness, and excellent resistance to fatigue and corrosion. One of the main concerns for using AM parts for safety-critical components is the presence of defects. While these defects have little or no effect on the static strength, they cause a significant reduction in the ductility and fatigue properties [1,2]. The surface roughness of AM metal parts is also a concern for structural integrity [3]. Studies have shown that surface roughness can be quantified and represented as micro notches or defects that can lead to localised stress concentration and result in fatigue strength reduction [3,4]. However, some parts are used in their as-built conditions, e.g. lattice structures or other complex geometries, which are impossible to machine and polish; some parts may have shorter design life or are subjected to lower applied stress, hence surface roughness may not be a problem. Moreover, one of the advantages of AM is to build near-net-shaped parts without or with much reduced post-process machining, as machining will increase the overall manufacturing cost.

To understand and quantify the impact of surface roughness on structural integrity, considerable research has been carried out on the tensile and fatigue properties of AM Ti64 [5–10]. The traditional stress-based approach using the material *S-N* data and notch stress has been used for predicting fatigue life reduction caused by surface roughness [6,11–13]. Recent research has also demonstrated that the fracture mechanics approach can be used for predicting the durability of AM parts due to initial damage of small size [14–18]. In the latter approach, the equivalent initial damage size (EIDS) concept was used as the initial crack length, and the material's crack growth rate property was used to calculate the fatigue life of the component. It is worth noting that EIDS values determined by Airbus for AM titanium alloys are around 0.25 mm for selective laser melted Ti64 with heat treatment and 0.45 mm for electron beam melted Ti64 [19]. It is consistent with a statement from the company that for as-built AM parts, EIDS rarely exceeds 0.5 mm [20].

* Corresponding author.
E-mail address: xiang.zhang@coventry.ac.uk (X. Zhang).

https://doi.org/10.1016/j.engfracmech.2021.107876
Received 19 February 2021; Received in revised form 15 June 2021; Accepted 5 July 2021
Available online 10 July 2021

Nomenclature

a, c	Crack length
A	Cyclic fracture toughness
B	Thickness of compact tension sample
D, p	Material constants in modified Hartman-Schijve equation
E	Young's modulus
K	Stress intensity factor
ΔK	Stress intensity factor range
K_c	Fracture toughness
K_{max}	Maximum stress intensity factor
ΔK_{th}	Threshold of ΔK for long crack
ΔK_{thr}	Crack length-dependent ΔK threshold
R	Cyclic load ratio
t	Thickness of small crack sample
W	Sample width
μ	Shear modulus
υ	Poisson's ratio

Abbreviations

EIDS	Equivalent initial damage size
LEFM	Linear elastic fracture mechanics
LC	Long crack
ND	Normal direction (Fig. 1)
SC	Small crack
SIF	Stress intensity factor
TD	Transverse direction (Fig. 1)
WD	Welding torch direction (Fig. 1)
3PB	Three-point bending (test)

Defects, surface roughness features and EIDS values are all in the sub-millimetre range, and it has been shown that using long crack growth rate data can overestimate the fatigue life as the cracks initiating from defects or surface roughness are in the small crack domain, which grows faster than long cracks under the same value of applied stress intensity factor [21–23]. Furthermore, fatigue cracks of relevance to many structural applications are often small or short, and a significant portion of fatigue life is spent in growing small cracks [24]. Therefore, when adopting the fracture mechanics approach for durability analysis, there is a need for small crack growth rate data. Owing to the absence of a standardised approach for small crack growth test and the time and cost constraints in testing small cracks, designers for aerospace structures often do not test small crack propagation behaviour [25]. Hence, for durability analysis of conventional and AM materials, empirical models representing the small crack growth behaviour by testing only the long crack specimens have been proposed [26–29].

The modified Hartman-Schijve equation proposed by Jones et al. [27] is shown to be able to predict a small crack growth rate for a range of aerospace and rail materials tested at a variety of R ratios [18,25–27,30]. Aiming to verify the modified Hartman-Schijve equation in a wire-based AM titanium alloy Ti64, the small crack test was conducted following the guidance given by ASTM E647 standard for testing small cracks in its appendix X3 [24]. Small crack growth behaviour was monitored, and its growth rate was measured. Material constants in the modified Hartman-Schijve equation were obtained from long crack test data. Predicted small crack growth life was validated by the small crack test data. Finally, the verified predictive model was used to predict the fatigue life of another configuration: a beam specimen built by AM process and tested under three-point bending fatigue load. Small crack growth from the as-built surface was monitored in the test and predicted to demonstrate the capability of the modified Hartman-Schijve equation.

2. Experimental method

The wire + arc additive manufactured (WAAM) Ti64 wall was deposited on a 12 mm thick forged Ti64 substrate using a grade-5 Ti64 wire of 1.2 mm diameter and plasma arc as an energy source. Argon gas of 99.99% purity was used as a shielding envelope (placed ahead of the torch and at the trailing end of the torch), directed precisely at the melt pool to avoid oxidation. A single bead deposition strategy was used to build a wall of 300 mm × 150 mm × 8 mm (thickness). The schematic of the wall is shown in Fig. 1a, from which two types of specimens were extracted for long crack and small crack testing.

For the long crack growth testing, two compact tension (C(T)) samples were extracted with a crack starter notch parallel to the weld direction. The geometry and dimension of the C(T) specimen are shown in Fig. 1b. The test was performed according to the ASTM E647 standard [24] at a constant amplitude sinusoidal load form with a maximum applied load of 3 kN, cyclic load ratio of 0.1 and a loading

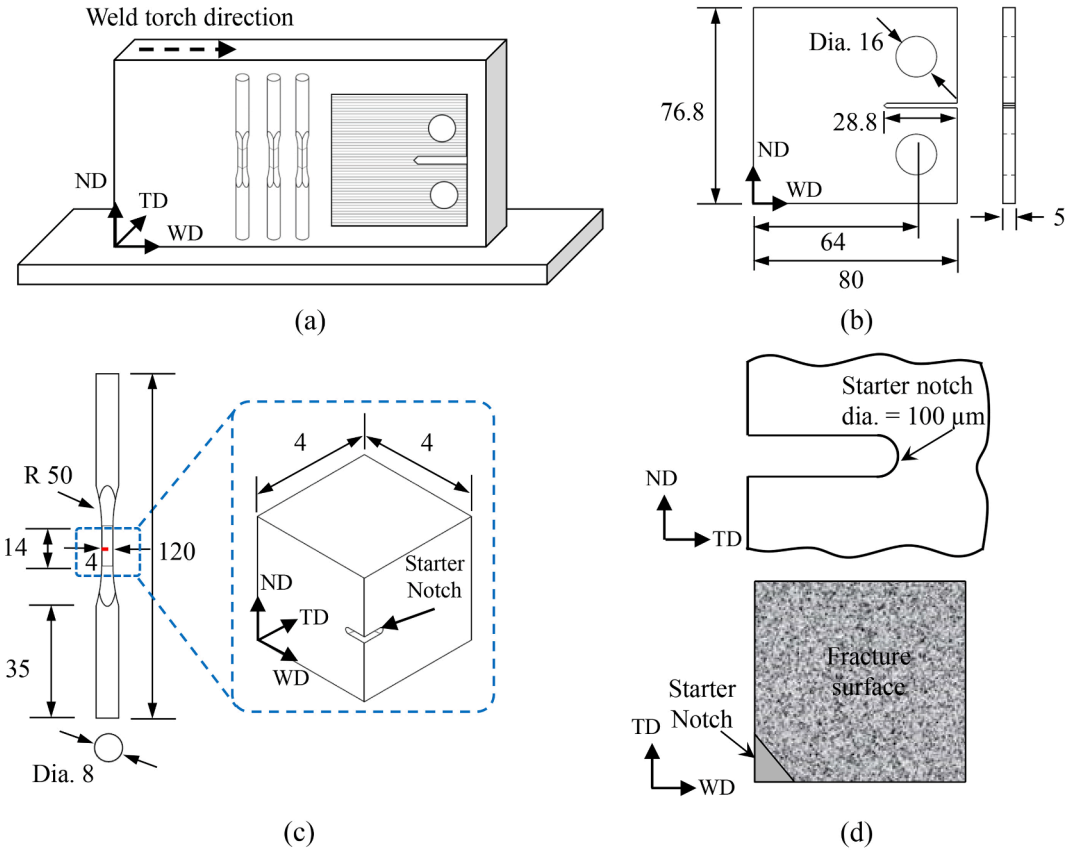

Fig. 1. (a) Schematic of the WAAM Ti64 wall showing welding torch movement direction and sample extraction plan, (b) compact tension specimen for a long crack test, (c) small crack sample and starter notch, (d) the starter notch. [WD: welding torch movement direction, TD: transverse (thickness) direction, ND: normal direction. Unit: mm, not to scale.]

frequency of 10 Hz. The crack length was measured using a travelling microscope with a 7 × objective lens, having an accuracy of ±0.01 mm. After the test, the seven point incremental polynomial procedure recommended in ASTM E647 standard [24] was used to calculate the crack growth rate from the measured data of crack length versus load cycles.

Small crack samples were also extracted (Fig. 1a, 1c) for measuring the crack growth rate in the sub-millimetre crack length range. The sample was designed according to ASTM E647 recommendations in Appendix X3 [24]. The following procedure was used to prepare the small crack samples for fatigue testing. First, the gauge section was polished using SiC paper up to 4000 grit size. A notch was then made using Electrical Discharge Machining (EDM) with a width and notch root diameter of 100 μm at the corner of the ND-WD and ND-TD planes (Fig. 1c, 1d). The notch size was between 0.4 and 0.7 mm. The gauge section was subsequently polished to a mirror finish, followed by etching using Kroll's reagent to reveal the microstructure.

Fatigue test on the small crack samples was conducted under applied load range of 2 and 3.2 kN, respectively, for the two samples, at a cyclic load ratio 0.1 and test frequency of 20 Hz. The fatigue test was paused at regular intervals to measure the crack length in both crack fronts on the TD-ND and WD-ND planes using a replication method [31]. An optical microscope was employed to measure the crack length from the replicas and observe the crack trajectory. For each sample, 40–50 replica measurements were taken. The reported crack length includes the initial notch size, and the final crack length recorded was in the range of 2–2.5 mm. After the fatigue test, the lead crack was identified from the replica at different cycle intervals, and the crack path was backtracked at specific cycle intervals. The seven point incremental polynomial method was used to calculate the crack growth rate from the measured data of crack length vs. load cycles. Fracture surfaces were examined using scanning electron microscopy (SEM) to identify the crack propagation pattern and fracture mechanisms.

3. Calculation of the stress intensity factors

For the compact tension specimen, the stress intensity factor K was calculated by Eq. (1) provided by ASTM E647 [24]:

$$K = \frac{P}{B\sqrt{W}} \frac{(2 + a/W)}{(1 - a/W)^{3/2}} (0.866 + 4.64(a/W) - 13.32(a/W)^2 + 14.72(a/W)^3 - 5.6(a/W)^4) \quad (1)$$

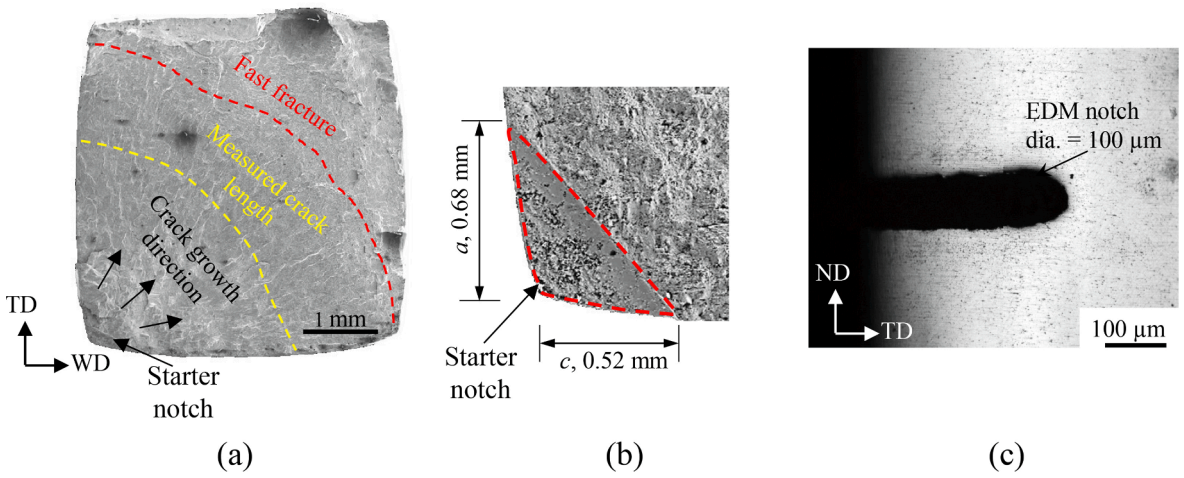

Fig. 2. (a) Secondary electron SEM image of a typical fracture surface of the small crack sample showing the EDM starter notch, crack initiation location from the notch, crack propagation direction, and fast fracture region, (b) Higher magnification image of the starter notch and dimensions, (c) optical microscopy image of the starter notch before the start of the test.

where P is the applied load, B sample thickness, W sample width, and a the crack length.

For calculating the stress intensity factor K of the small crack (SC) test sample, the aspect ratio (a/c) of the corner crack was measured from the fracture surface shown in Fig. 2, which was 1.01 for sample SC-Test-1, and 1.35 for SC-Test-2. The starter notch was triangular shaped with a notch root curvature of 0.1 mm diameter (Fig. 2c). Beyond crack extension length of about 0.7 mm, crack shape became quarter-elliptical or near quarter-circular (Fig. 2a). Therefore, the K value was calculated by the Newman-Raju formulae [32] shown here as Eqs. (2)–(4).

$$K = S\sqrt{\frac{\pi a}{Q}}F_c\left(\frac{a}{c}, \frac{a}{t}, \phi\right) \tag{2}$$

$$F_c = \left[M_1 + M_2\left(\frac{a}{t}\right)^2 + M_3\left(\frac{a}{t}\right)^4\right] g_1 g_2 f_\varnothing \tag{3}$$

$$Q = 1 + 1.464\left(\frac{c}{a}\right)^{1.65}, a/c > 1 \tag{4}$$

where S is the applied stress perpendicular to the crack plane, a and c the crack lengths as marked in Fig. 2b, b and t the width and thickness of the sample, Q the shape factor, F_c the boundary correction factor, g_i and M_i the curve fitting functions, and ϕ the angular function. Detailed calculation procedure can be found in [32].

However, the Newman-Raju equation for quarter-elliptical corner crack [32] can overestimate the K value for samples tested in this study due to the differences in the starter notch shape. Hence, the finite element (FE) modelling was also conducted in this study. The FE model was firstly verified with the Newman-Raju model [32] for a quarter-elliptical notch before being applied for the notch shape of the test samples used in this study. The ABAQUS software package was used for the FE models [33].

FE model of one-half of the sample is shown in Fig. 3a. The quadric tetrahedron elements were used with refined mesh around the notch root curvature and the extended crack front (Fig. 3b). Contour maps of the stress component in the loading direction (noted as S33) are shown in Fig. 3c and 3d. The linear elastic fracture mechanics (LEFM) approach was then followed to calculate the K value using the displacement extrapolation method [34]. Under the Mode I load and using the cylindrical coordinate system (r, θ), the relationship between K and the displacement component in the loading direction v is given by Eq. (5)

$$v = \frac{K_I}{4\mu}\sqrt{\frac{r}{2\pi}}\left[(2\kappa + 1)sin\frac{\theta}{2} - sin\frac{3\theta}{2}\right] \tag{5}$$

Material constants κ and μ are functions of the elastic properties; $\kappa = (3\text{-}\upsilon)/(1 + \upsilon)$ (plane strain), $\kappa = 3\text{-}4\upsilon$ (plane stress), and shear modulus $\mu = E/2(1 + \upsilon)$.

In this study, crack length refers to the crack size at the sample surface (crack length "a" in Fig. 2b). Therefore, the plane stress condition was used for calculating the K values. For $\theta = 180°$, Eq. (5) is expressed as Eq. (6)

$$K = \frac{Ev}{4}\sqrt{\frac{2\pi}{r}} \tag{6}$$

Using value 0.3 for the Poisson's ratio in Eq. (5), the ratio of plane-stress K (for a crack at the plate surface) over plane-strain K

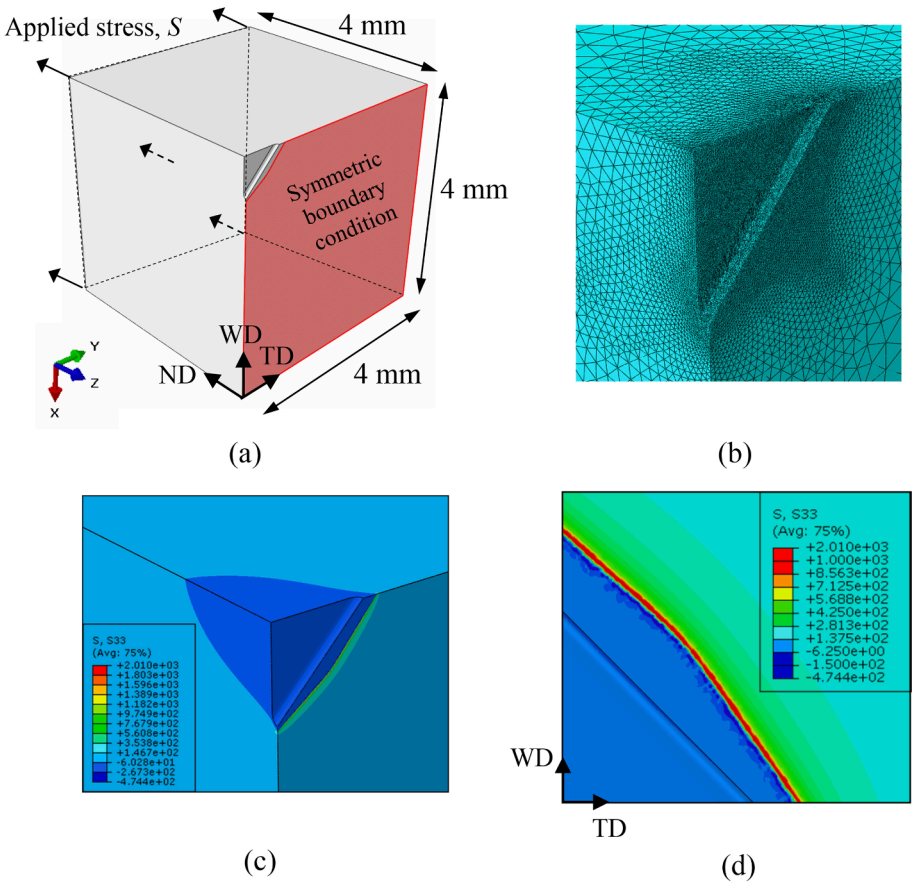

Fig. 3. Finite element model of one-half of the test sample: (a) starter notch with a small crack extension of 0.1 mm, load and boundary conditions, (b) FE model, (c) and (d) contour maps of stress in load direction (S_{33}). Applied stress was 150 MPa for this illustration.

(crack length at the point of maximum crack penetration) is 0.91. This ratio factor was originally proposed by Jolles & Tortoriello with a value of 0.91 and was related to the crack closure differences at the two crack locations [35]. It is essentially the same argument based on the variation in the constraint along the crack border, from plane stress at the plate surface to that of plane strain at the point of maximum crack penetration. This ratio factor was proposed to improve life prediction accuracy based on early studies on crack growth predictions of semi-elliptical surface and quarter-elliptical corner cracks that demonstrated that the crack growth could not be predicted solely by stress intensity factor ranges [35,36]. To account for this difference, Jolles and Tortoriello [35] multiplied the stress intensity factor range at the free surface by a factor of 0.91, and Newman and Raju [36] used a factor of 0.9.

FE calculated K is presented in Fig. 4 and compared with the Newman-Raju analytical solution. It shows that the K values for cracks

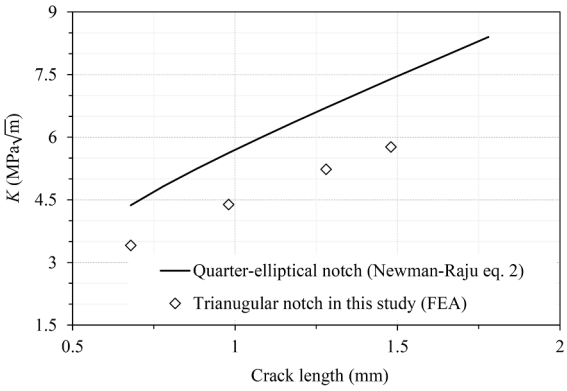

Fig. 4. Calculated stress intensity factor for the small crack sample with initial notch being modelled as quarter-elliptical shape (Newman-Raju Eq. (2)) or triangular shape (FEA, Fig. 1d). Applied stress is 150 MPa, crack length including notch size.

extended from the triangular-shaped starter notch were about 22% lower than the Newman-Raju solution for cracks extended from a quarter-elliptical starter notch. The FE work also modelled the notch root curvature of a 0.1 mm diameter in the test samples (Fig. 2c) that resulted from the wire-EDM cut, whereas the Newman-Raju analytical method assumes a sharp notch root, i.e. without a curvature front [32]. Therefore, K values calculated by Newman-Raju equation were reduced by a factor of 0.78.

4. Representing small crack growth rate by the modified Hartman-Schijve equation

4.1. Measurement of small crack growth rate

Two samples were tested, noted as specimen SC-Test-1 and SC-Test-2. The propagation of the lead crack in the ND-TD plane is shown in Fig. 5. Crack branching and crack coalescence were also observed in both tests. In SC-Test-1, a secondary crack initiated after about 1.2×10^6 cycles, which later joined the lead crack and continued the trend until failure (Fig. 5a). In SC-Test-2, the lead crack grew continuously until fracture, with only a slight crack deviation and branching being observed (Fig. 5b).

Projected crack lengths of the dominant crack were plotted against the load cycle numbers in Fig. 6a, where SC-Test-2 had a higher applied stress range (180 MPa), and the sample failed earlier than SC-Test 1 (applied stress range 135 MPa). The crack growth rates of both samples are comparable as they are governed by the stress intensity factor, Fig. 6b. Data reduction was performed by the 7-point polynomial method as recommended by the ASTM E647 standard. It was observed that in the area of the starter notch the crack was deflected and bifurcated in both samples. Secondary cracks were also observed, and they later joined the dominant crack (Fig. 5, near to the starter notch). The crack bifurcation and secondary crack formation reduced the crack growth rate in the early stage of crack growth. The crack growth rate increased rapidly after the crack length exceeded 0.75 mm. In general, small crack growth is affected by the variations in the microstructure and crystallographic texture at the crack front [23,37,38]. If a small crack is encountered with different orientations of crystallographic texture at the crack front, it may deviate from its path and grow in the favourable direction governed by local slip systems [38].

Calculated small and long crack growth rates are plotted together in Fig. 7. It shows that small cracks had higher growth rates than the long cracks at the same applied ΔK. The difference in crack growth rates is associated with the difference in constraints imposed by the elastic material surrounding the crack, which may be different in small cracks [39]. The constraint exerted at small cracks initiating from or growing on a free surface of smooth samples is different from the through-thickness long crack in the same material [35]. Therefore, even when the loading condition and the crack size satisfy the requirement of LEFM, the physical smallness of the crack generates faster crack growth rates. Long cracks with longer plastic wake will slow down the crack growth rate further [39].

Moreover, the small cracks are comparable to the α colony size of WAAM Ti64 and are hence affected by the crystallographic orientation of the grains [40,41]. Consequently, local plastic zone sizes are different from the long fatigue cracks [39]. These microstructural and crystallographic orientations have a substantially diminished effect on the growth of long cracks [39,42]. In the case of long cracks, the crack tip interacts with a larger number of grains; hence the bulk material properties govern the fracture behaviour. Furthermore, small cracks do not have the crack closure effect, further increasing the crack growth rate under the same applied ΔK.

4.2. Modified Hartman-Schijve equation

Some well-known equations describing the fatigue crack growth rate are mentioned here as they lead to the modified Hartman-

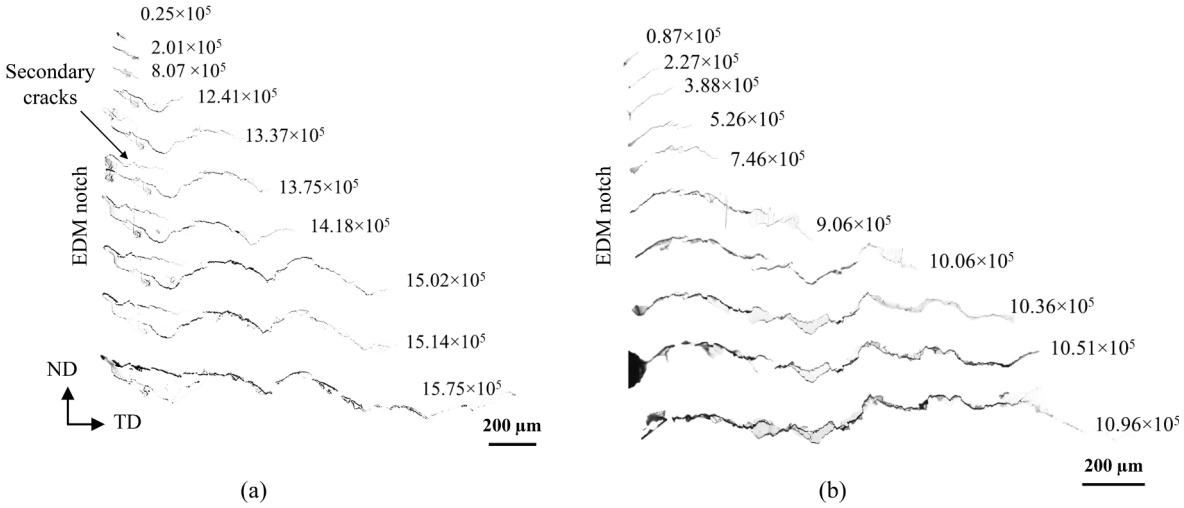

Fig. 5. Measurement of the lead crack trajectories by replication method in the small crack (SC) samples; (a) SC-Test-1 under applied stress range 135 MPa, (b) SC-Test-2 under applied stress range 180 MPa. Crack growth was along the TD direction (Fig. 1).

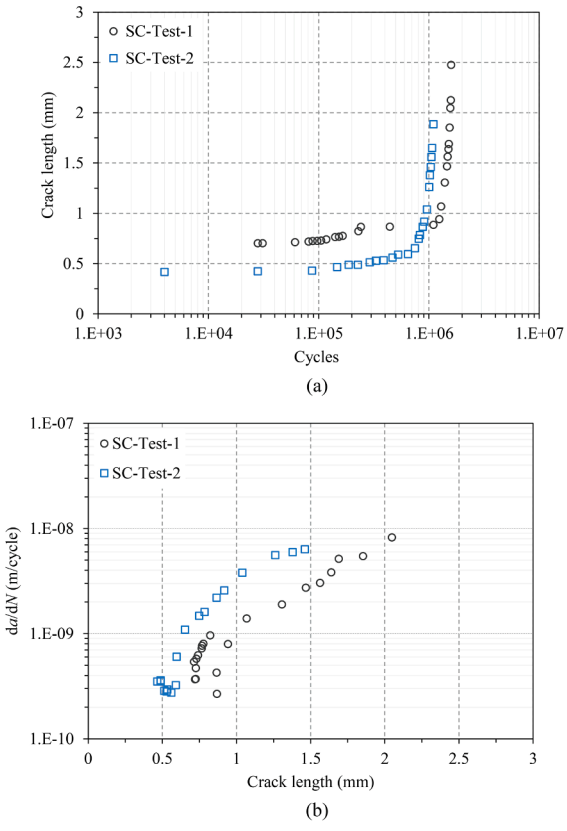

Fig. 6. Result of small crack test: (a) a vs. N; crack length was measured by replication of the dominant crack and projected crack length is plotted here, (b) da/dN vs. a (crack length includes the starter notch).

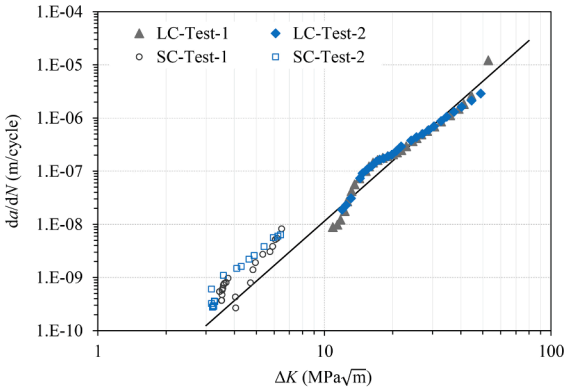

Fig. 7. da/dN vs. ΔK for the long crack (LC) and small crack (SC) samples tested in this study. The long crack data trend line (solid line) shows small cracks growing faster under the same applied ΔK.

Schijve equation proposed by Jones et al. [27] that is used in this study. The Paris law was the first to establish the relationship between da/dN and ΔK by a power function [43]:

$$\frac{da}{dN} = C(\Delta K)^m \tag{7}$$

where C and m are material constants. However, it does not account for the R ratio effect nor the asymptotic trend in the ΔK_{th} and the fast crack growth regions. Improved functions have been proposed in the literature to overcome these limitations.

The Forman law in Eq. (8) [44] accounts for the R ratio effect, and the term $[(1\text{-}R)K_C - \Delta K]$ predicts the asymptotic behaviour when crack growth rate goes to infinity, and ΔK approaches the fracture toughness, K_C.

$$\frac{da}{dN} = \frac{C(\Delta K)^m}{[(1-R)K_c - \Delta K]} \tag{8}$$

The ΔK_{th} asymptote was later included in the Forman equation by Hartman-Schijve [45] by changing the numerator to (ΔK - ΔK_{th}), Eq. (9). A similar equation was also proposed by Priddle [46].

$$\frac{da}{dN} = \frac{C(\Delta K - \Delta K_{th})^m}{[(1-R)K_c - \Delta K]} \tag{9}$$

Jones et al. [27] modified the original Hartman-Schijve equation, Eq. (9), to the form of Eq. (10). They later referred it as a variant of the NASGRO equation [18,27,30,47] because the constant q in the original NASGRO equation was set as $p/2$ in Eq. (10). Caton et al. [48] observed that there was no discernible effect of R ratio on small crack growth rate if plotted as a function of ΔK. Therefore, Hartman-Schijve equation has been used for small crack problems [5,17].

$$\frac{da}{dN} = D\left(\frac{\Delta K - \Delta K_{thr}}{\sqrt{1 - K_{max}/A}}\right)^p \tag{10}$$

In Jones' papers [17,18,30,49], Eq. (10) is written in a simpler form as Eq. (11), where the $\Delta\kappa$ parameter was proposed by Schwalbe [50], Eq. (12),

$$\frac{da}{dN} = D(\Delta\kappa)^p \tag{11}$$

$$\Delta\kappa = \frac{(\Delta K - \Delta K_{thr})}{\sqrt{1 - K_{max}/A}} \tag{12}$$

where D and p are material constants, A the cyclic fracture toughness, and ΔK_{th} the fatigue crack growth threshold that is dependent on the microstructure and the R ratio. For small cracks, ΔK_{th} is termed as ΔK_{thr} in Jones' papers [18,30,49] to distinguish it from the long crack K threshold values. They proposed that the small crack growth behaviour can be represented from the long crack test data by

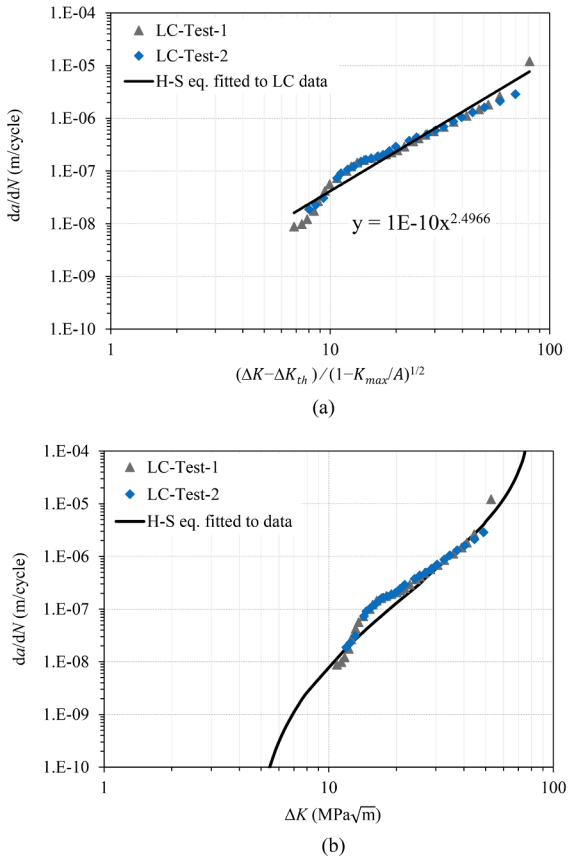

Fig. 8. Hartman-Schijve equation fitted to long crack test data: (a) da/dN vs. $\Delta\kappa$ for determining material constants D and p by the fitting curve, (b) da/dN vs. ΔK. Material data used in Eq. (11): A = 90 MPa$\sqrt{\text{m}}$ and ΔK_{th} = 4.5 MPa$\sqrt{\text{m}}$.

setting the ΔK_{thr} to a very small value of around 0.1–0.3 MPa$\sqrt{m}$ [18,49].

In this paper, long crack growth rate da/dN is plotted against $(\Delta K - \Delta K_{thr})/\sqrt{1 - K_{max}/A}$ in a log-log graph in Fig. 8a, where parameter A is the stress intensity factor range at failure under fatigue load. As the first estimation, the value of A should be closer to the fracture toughness property value under static load as the term K_c in the original Forman equation, Eq. (8). In [51], the fracture toughness value for WAAM single bead Ti64 was measured as 70–81 MPa$\sqrt{m}$, and in [17] an average value of 75.5 MPa$\sqrt{m}$ was measured for another additive manufactured Ti64. In the threshold-K region, da/dN is not sensitive to assumed A values in the range of 70–90 MPa$\sqrt{m}$. The value of ΔK_{thr} was subsequently chosen to make da/dN vs.$(\Delta K - \Delta K_{thr})/\sqrt{1 - K_{max}/A}$ plot in the near threshold region appears as a straight line. The value of A was then further adjusted to improve the linearity of the plot in the high ΔK region. This process generally results in very slight difference in the da/dN vs. $(\Delta K - \Delta K_{thr})/\sqrt{1 - K_{max}/A}$ plots in the high ΔK region. Hence, the value of A was estimated to be 90 MPa$\sqrt{m}$. It can be seen in Fig. 8b that the modified Hartman-Schijve equation can well represent the crack growth rate of the long cracks with values $A = 90$ MPa$\sqrt{m}$ and long crack threshold $\Delta K_{th} = 4.5$ MPa$\sqrt{m}$ [2]. The material constants were calculated as $D = 1 \times 10^{-10}$ and $p = 2.49$, in units of MPa and m, through the linear fitting of the test data with an $R^2 = 0.96$ (Fig. 8a).

Using Eq. (11), fitted da/dN vs. applied ΔK is presented in Fig. 8b and compared with test measured long crack growth data. Moreover, Eq. (11) also describes the asymptotic behaviour in the threshold and fast crack growth regions. Note, stress intensity factor threshold for long cracks ΔK_{th} used for this fitting is 4.5 MPa$\sqrt{m}$.

The small crack growth rate was then predicted using Eq. (11), using material constants D and p obtained from long crack test data (Fig. 8a) and a smaller ΔK_{th} value based on findings in [23,48,51,52], where the value of ΔK_{th} was set much smaller than the long crack threshold value in order to make small cracks grow. In Jones' papers [17,18,30,49], this small crack growth threshold was noted as ΔK_{thr}, and small crack da/dN vs. ΔK was approximated by setting the ΔK_{thr} to a very small value of 0.3 MPa$\sqrt{m}$. Values suggested by [17,18,30] may be suitable for microstructurally small cracks but may be impractical for small cracks initiated from defects found in WAAM Ti64 as work in [23,48,52] found higher ΔK_{thr} values for small cracks in Ti64 as 1.8–3.0 MPa$\sqrt{m}$. A sensitivity study of ΔK_{thr} value was performed in this study. Fig. 9 shows that higher ΔK_{thr} value (e.g. using the long crack threshold value 4.5 MPa$\sqrt{m}$) resulted in delayed crack growth onset and slower crack growth rate under the same ΔK compared to $\Delta K_{thr} = 3$ MPa$\sqrt{m}$. Lower ΔK_{thr} start the crack growth earlier and increase the crack growth rate. Fig. 9 supports the hypothesis that the Hartman-Schijve equation, Eq. (11), with appropriate values of A and ΔK_{thr} gives reasonable approximation of the small crack growth rate as supported by the test data. Therefore, in this study, $\Delta K_{thr} = 2$ MPa$\sqrt{m}$ was used in Eq. (11) for predicting the small crack growth rate in the selected material, which is validated by small crack test data in this study.

Fig. 9 shows good agreement between the predicted and test measured crack growth rates for the small crack specimens. It also shows a good comparison with the work performed by Jones et al. [30] on a Ti64 alloy made by selected laser melting (SLM) process, using $D = 2.79 \times 10^{-10}$ and $p = 2.12$ in Eq. (11).

5. Predicting fatigue life of a WAAM Ti-6Al-4V part in as-built surface condition

To further demonstrate the capability of Eq. (11), the effect of surface roughness on the fatigue life of a WAAM Ti64 specimen was studied under the three-point bending load. Crack initiation from surface waviness features and small crack growth behaviour were monitored during the fatigue test and predicted.

Specimen geometry and dimension are shown in Fig. 10c. First, the surface waviness was quantified using a form tracer of Mitutoyo FT SV-C3200/4500 series. A stylus of 4 μm diameter with a diamond tip was used with an applied force of 5 mN on the stylus to keep contact with the surface (Fig. 10). Details can be found in [53]. Fig. 10c shows the beam specimen with the as-built surface on one side (the tension side) and the machined surface on the other side. In this study, each of the waviness trough is referred to as a "notch", so the crack initiating "notch" is in the mid-span of the beam sample, as shown in Fig. 10d. For fatigue life prediction, the EIDS concept was used to define the initial crack size, which was the depth of the centre notch. For the WAAM Ti64 as-built surface studied here,

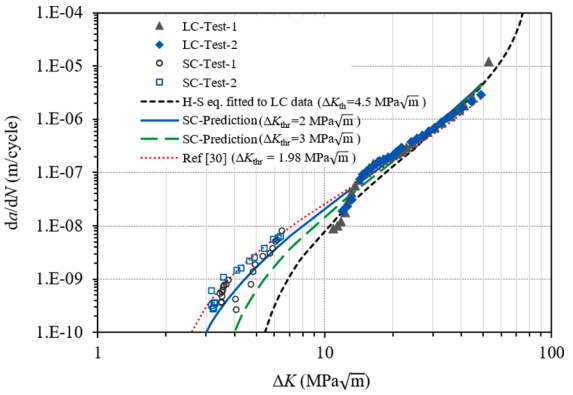

Fig. 9. Prediction of small crack growth rate using long crack data fitted Hartman-Schijve equation with $\Delta K_{thr} = 2$ and 3 MPa$\sqrt{m}$, and comparison with Hartman-Schijve equation for SLM Ti64 [30].

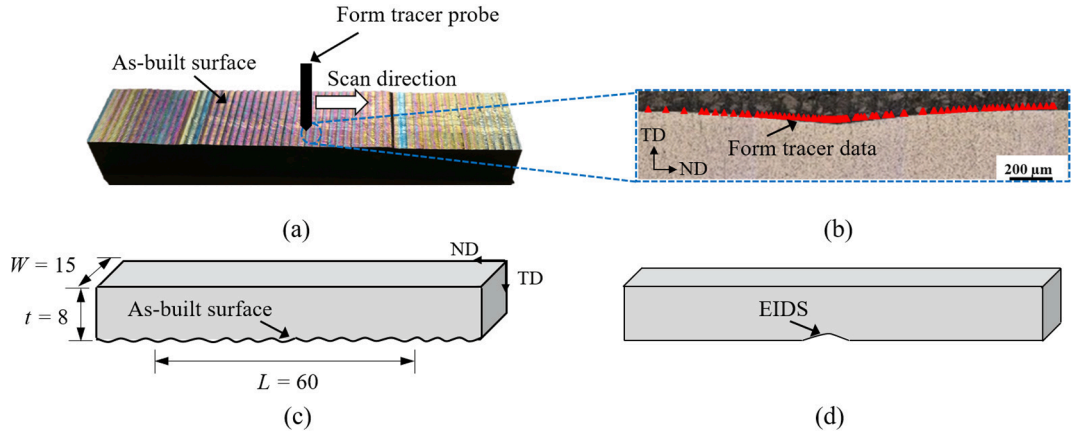

Fig. 10. (a-b) measurement of the surface waviness and "notch" size on a WAAM Ti64 specimen using the form tracer metrology technique, (c) a beam sample for fatigue test, (d) model of the "centre notch" in the beam specimen; notch depth is treated as equivalent initial damage size (EIDS).

EIDS ranged 0.05–0.32 mm, i.e. the initial cracks were sub-mm small cracks.

To aid crack growth monitoring and measurement, the ND-TD plane was ground and polished using SiC paper and polished up to 0.06 μm silica suspension and subsequently etched using Kroll's reagent for approx. 45 s. The experimental setup for the three-point bending test is shown in Fig. 11a. The fatigue test was performed under constant amplitude load in a sinusoidal waveform with a cyclic load ratio of 0.1 and 10 Hz loading frequency. The as-built surface was facing downwards, where the maximum applied bending stress S_{max} was calculated by Eq. (13) [54].

$$S_{max} = \frac{3PL}{2Wt^2} \tag{13}$$

where P is the applied load, L the distance between the supporting rollers (beam span = 60 mm), W the width (15 mm) and t the thickness (8 mm), Fig. 10c. Fatigue testing was paused at every 20,000 cycles to monitor the crack initiation from the centre notch using a travelling microscope until the initiation of a small crack. After that, crack length was measured at every 2000 cycles until it reached a length of about 1.6 mm, see Fig. 11b.

Equations for calculating the stress intensity factor K for a beam under three-point bending load can be found in [55,56]. Solutions provided by these references are comparable. Therefore, Eq. (14) from [55] was used in this study.

$$K = \frac{PL}{Wt^{3/2}}\left[2.9\left(\frac{a}{t}\right)^{1/2} - 4.6\left(\frac{a}{t}\right)^{3/2} + 21.8\left(\frac{a}{t}\right)^{5/2} - 37.6\left(\frac{a}{t}\right)^{7/2} + 38.7\left(\frac{a}{t}\right)^{9/2}\right] \tag{14}$$

where P is applied load, L the distance between the supporting rollers, W the sample width, t the sample thickness, and a the crack length in TD direction (Fig. 11b).

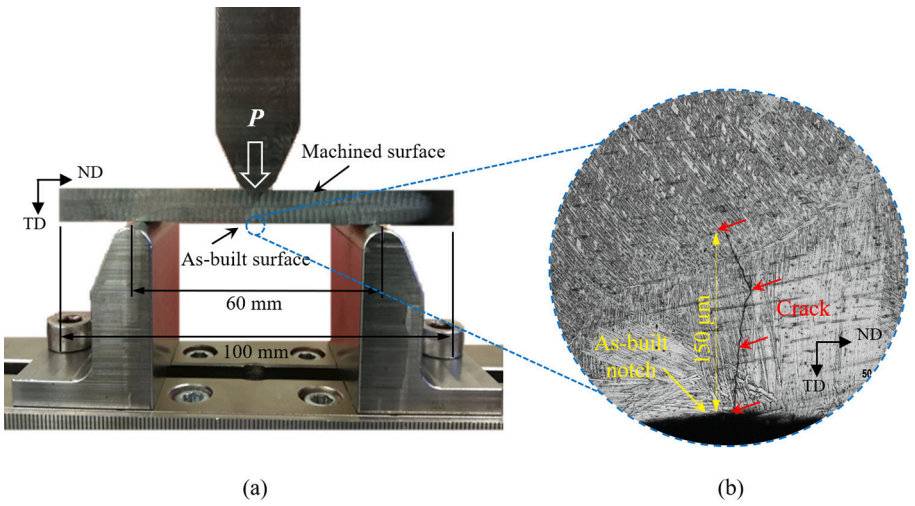

Fig. 11. (a) Experimental setup of three-point bending fatigue test; (b) optical microscopy image showing crack initiating from the centre notch and small crack propagation.

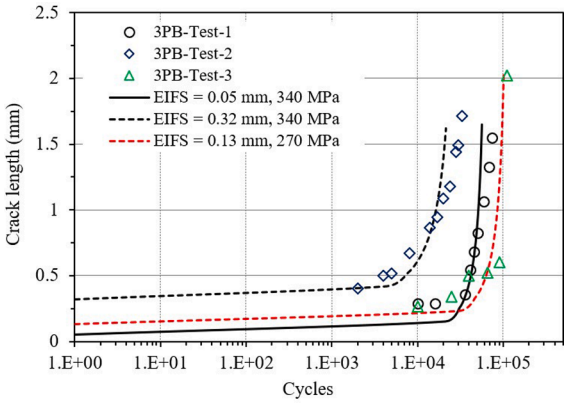

Fig. 12. Predicted fatigue life for beam specimen with as-built surface condition based on the small crack growth approach.

The fatigue life was calculated by numerical integration of Eq. (11) using material constants given in Section 4. Fig. 12 shows the comparison of prediction with test measurement. Two EIDS values were used as the initial crack length, 0.05 and 0.32 mm, for specimens tested at stress range of 340 MPa (3PB-Test-1, 3PB-Test-2) and EIDS = 0.13 mm for the third specimen tested at 270 MPa (3PB-Test-3). The experimental test result shows that specimen 3PB-Test-2 failed earlier than 3PB-Test-1 at the same applied stress range. The predicted fatigue life range based on the shallowest and deepest notch sizes (0.05 and 0.32 mm) covered the experimental test data range and can be regarded as a good prediction.

6. Conclusions

The purpose of this work was to establish a unified crack growth rate law to represent both the long crack and small crack regimes using the modified Hartman-Schijve equation and long crack test data. The representation of small crack growth rate was validated by testing small crack samples and another geometry with crack initiating and propagating from as-built surface waviness. The following conclusions can be drawn:

- The modified Hartman-Schijve equation can be used as a unified crack growth rate law to represent both small and long crack growth rates; the material constants can be determined by testing standard long crack specimens.
- The surface waviness of as-built WAAM Ti64 can be characterised as an array of micro notches; the notch depth can be modelled as the equivalent initial damage size (EIDS) or initial crack size.
- The durability life of the beam specimen with as-built surface condition can be predicted by the fracture mechanics approach using the modified Hartman-Schijve equation and the equivalent initial damage size (EIDS) as the initial crack length.

Declaration of Competing Interest

The authors declare that they have no known competing financial interests or personal relationships that could have appeared to influence the work reported in this paper.

Acknowledgement

The authors thank Cranfield University for providing experimental materials. MS also thanks the WAAMMat programme and Coventry University for PhD studentship. XZ thanks the Engineering and Physical Science Research Council (EPSRC) for supporting this research through the NEWAM programme grant (EP/R027218/1).

References

[1] Liu F, He C, Chen Y, Zhang H, Wang Q, Liu Y. Effects of defects on tensile and fatigue behaviors of selective laser melted titanium alloy in very high cycle regime. Int J Fatigue 2020;140:105795. https://doi.org/10.1016/j.ijfatigue.2020.105795.
[2] Biswal R, Zhang X, Syed AK, Awd M, Ding J, Walther F, et al. Criticality of porosity defects on the fatigue performance of wire + arc additive manufactured titanium alloy. Int J Fatigue 2019;122:208–17. https://doi.org/10.1016/j.ijfatigue.2019.01.017.
[3] Townsend A, Senin N, Blunt L, Leach RK, Taylor JS. Surface texture metrology for metal additive manufacturing: a review. Precis Eng 2016;46:34–47. https://doi.org/10.1016/j.precisioneng.2016.06.001.
[4] Fousová M, Vojtěch D, Doubrava K, Daniel M, Lin CF. Influence of inherent surface and internal defects on mechanical properties of additively manufactured Ti6Al4V alloy: Comparison between selective laser melting and electron beam melting. Materials (Basel) 2018;11. Doi: 10.3390/ma11040537.
[5] Nourian-Avval A, Fatemi A. Fatigue life prediction of cast aluminum alloy based on porosity characteristics. Theor Appl Fract Mech 2020;109:102774. https://doi.org/10.1016/j.tafmec.2020.102774.
[6] Guilherme AS, Pessanha Henriques GE, Zavanelli RA, Mesquita MF. Surface roughness and fatigue performance of commercially pure titanium and Ti-6Al-4V alloy after different polishing protocols. J Prosthet Dent 2005;93:378–85. https://doi.org/10.1016/j.prosdent.2005.01.010.

[7] Chan KS, Koike M, Mason RL, Okabe T. Fatigue life of titanium alloys fabricated by additive layer manufacturing techniques for dental implants. Metall Mater Trans A 2013;44:1010–22. https://doi.org/10.1007/s11661-012-1470-4.
[8] Persenot T, Burr A, Martin G, Buffiere JY, Dendievel R, Maire E. Effect of build orientation on the fatigue properties of as-built Electron Beam Melted Ti-6Al-4V alloy. Int J Fatigue 2019;118:65–76. https://doi.org/10.1016/j.ijfatigue.2018.08.006.
[9] Tato W, Blunt L, Llavori I, Aginagalde A, Townsend A, Zabala A. Surface integrity of additive manufacturing parts: a comparison between optical topography measuring techniques. Procedia CIRP 2020;87:403–8. https://doi.org/10.1016/j.procir.2020.02.082.
[10] Kahlin M, Ansell H, Basu D, Kerwin A, Newton L, Smith B, et al. Improved fatigue strength of additively manufactured Ti6Al4V by surface post processing. Int J Fatigue 2020;134:105497. https://doi.org/10.1016/j.ijfatigue.2020.105497.
[11] Edwards P, Ramulu M. Fatigue performance evaluation of selective laser melted Ti-6Al-4V. Mater Sci Eng A 2014;598:327–37. https://doi.org/10.1016/j.msea.2014.01.041.
[12] Bagehorn S, Wehr J, Maier HJ. Application of mechanical surface finishing processes for roughness reduction and fatigue improvement of additively manufactured Ti-6Al-4V parts. Int J Fatigue 2017;102:135–42. https://doi.org/10.1016/j.ijfatigue.2017.05.008.
[13] Nicoletto G. Anisotropic high cycle fatigue behavior of Ti–6Al–4V obtained by powder bed laser fusion. Int J Fatigue 2017;94:255–62. https://doi.org/10.1016/j.ijfatigue.2016.04.032.
[14] Sanaei N, Fatemi A. Defect-based multiaxial fatigue life prediction of L-PBF additive manufactured metals. Fatigue Fract Eng Mater Struct 2021:1897–915. https://doi.org/10.1111/ffe.13449.
[15] Sanaei N, Fatemi A. Defect-based fatigue life prediction of L-PBF additive manufactured metals. Eng Fract Mech 2021;244:107541. https://doi.org/10.1016/j.engfracmech.2021.107541.
[16] Jones R, Michopoulos JG, Iliopoulos AP, Singh Raman RK, Phan N, Nguyen T. Representing crack growth in additively manufactured Ti-6Al-4V. Int J Fatigue 2018;116:610–22. https://doi.org/10.1016/j.ijfatigue.2018.07.019.
[17] Iliopoulos AP, Jones R, Michopoulos JG, Phan N, Rans C. Further studies into crack growth in additively manufactured materials. Materials (Basel) 2020;13:5–10. https://doi.org/10.3390/ma13102223.
[18] Iliopoulos A, Jones R, Michopoulos J, Phan N, Singh Raman R. Crack growth in a range of additively manufactured aerospace structural materials. Aerospace 2018;5:118. https://doi.org/10.3390/aerospace5040118.
[19] Mardaras J, Emile P, Santgerma A. Airbus approach for F & DT stress justification of additive manufacturing parts. Procedia Struct Integr 2017;7:109–15. https://doi.org/10.1016/j.prostr.2017.11.067.
[20] Greitemeier D, Dalle Donne C, Syassen F, Eufinger J, Melz T. Effect of surface roughness on fatigue performance of additive manufactured Ti–6Al–4V. Mater Sci Technol 2015;32:1743284715Y.000. Doi: 10.1179/1743284715Y.0000000053.
[21] Lincoln JW, Melliere RA. Economic life determination for a military aircraft. vol. 36. 1999. Doi: 10.2514/2.2512.
[22] Zhai Y, Galarraga H, Lados DA. Microstructure, static properties, and fatigue crack growth mechanisms in Ti-6Al-4V fabricated by additive manufacturing: LENS and EBM. Eng Fail Anal 2016;69:3–14. https://doi.org/10.1016/j.engfailanal.2016.05.036.
[23] Zhai Y, Lados DA, Brown EJ, Vigilante GN. Fatigue crack growth behavior and microstructural mechanisms in Ti-6Al-4V manufactured by laser engineered net shaping. Int J Fatigue 2016;93:51–63. https://doi.org/10.1016/j.ijfatigue.2016.08.009.
[24] ASTM E647-15: Standard test method for measurement of fatigue crack growth rates 2015:1–49. Doi: 10.1520/E0647-15E01.2.
[25] Main B, Jones M, Barter S. The practical need for short fatigue crack growth rate models. Int J Fatigue 2021;142:105980. https://doi.org/10.1016/j.ijfatigue.2020.105980.
[26] Jones R, Molaei R, Fatemi A, Peng D, Phan N. A note on computing the growth of small cracks in AM Ti-6Al-4V. Procedia Struct Integr 2020;28:364–9. https://doi.org/10.1016/j.prostr.2020.10.043.
[27] Jones R, Molent L, Walker K. Fatigue crack growth in a diverse range of materials 2012;40:43–50. Doi: 10.1016/j.ijfatigue.2012.01.004.
[28] Schra RJHW and L. Short cracks and durability analysis of the Fokker 100 wing,fuselage structure. Short Fatigue Cracks 1992; ESIS 13:1–27.
[29] Papangelo A, Guarino R, Pugno N, Ciavarella M. On unified crack propagation laws. Eng Fract Mech 2019;207:269–76. https://doi.org/10.1016/j.engfracmech.2018.12.023.
[30] Jones R, Raman RKS, Iliopoulos AP, Michopoulos JG, Phan N, Peng D. Additively manufactured Ti-6Al-4V replacement parts for military aircraft. Int J Fatigue 2019;124:227–35. https://doi.org/10.1016/j.ijfatigue.2019.02.041.
[31] Qin CH, Zhang XC, Ye S, Tu ST. Grain size effect on multi-scale fatigue crack growth mechanism of Nickel-based alloy GH4169. Eng Fract Mech 2015;142:140–53. https://doi.org/10.1016/j.engfracmech.2015.06.003.
[32] Newman Jr JC, Raju IS. Stress-intensity factor equations for cracks in three-dimensional finite bodies. ASTM Spec Tech Publ 1983;1:238–65. https://doi.org/10.1520/stp37074s.
[33] ABAQUS, Analysis user's manual. Version 6.14, Dassault Systemes Simulia, Inc.; 2014.
[34] Anderson T. Chapter 2: Linear elastic fracture mechanics. Fract. Mech. Fundam. Appl. Third, Boca Raton: Taylor & Francis Group; 2005.
[35] Jolles M, Tortoriello V. Geometry variations during fatigue growth of surface flaws. ASTM STP 791 Fract Mech 1983:297–307.
[36] Newman Jr J, Raju I. Prediction of fatigue crack-growth pattern and lives in three-dimensional cracked bodies. International Congress on Fracture (ICF) 1984. https://doi.org/10.1016/B978-1-4832-8440-8.50151-4.
[37] Xie Y, Gong M, Luo Z, Li Q, Gao M, Wang F, et al. Effect of microstructure on short fatigue crack growth of wire arc additive manufactured Ti-6Al-4V. Mater Charact 2021:104743. https://doi.org/10.1016/j.matchar.2021.111183.
[38] Bantounas I, Lindley TC, Rugg D, Dye D. Effect of microtexture on fatigue cracking in Ti-6Al-4V. Acta Mater 2007;55:5655–65. https://doi.org/10.1016/j.actamat.2007.06.034.
[39] Chapter Suresh S. 15: Small fatigue cracks. Fatigue Mater. Second, New York: Cambridge University Press; 1998.
[40] Lutjering G. Engineerig Materials and Processes. Second. Hamburg: Springer; 2007.
[41] Shamir M, Syed AK, Janik V, Biswal R, Zhang X. The role of microstructure and local crystallographic orientation near porosity defects on the high cycle fatigue life of an additive manufactured Ti-6Al-4V. Mater Charact 2020;169:110576. https://doi.org/10.1016/j.matchar.2020.110576.
[42] Suresh S, Ritchie RO. Propagation of short fatigue cracks. Int Met Rev 1984;29:445–75. https://doi.org/10.1179/imtr.1984.29.1.445.
[43] Paris P, Erdogan F. A critical analysis of crack propagation laws. J Basic Eng 1963;85:528–1524.
[44] Forman R, Keary V, Engle R. Numerical analysis of crack propagation in cyclic-loaded structures. J Basic Eng 1967;89:459–64.
[45] Hartman A, Schijve J. The effects of environment and load frequency on the crack propagation law for macro fatigue crack growth in aluminium alloys. Eng Fract Mech 1970;1:615–31. https://doi.org/10.1016/0013-7944(70)90003-2.
[46] Priddle E. High cycle fatigue crack propagation under random and constant amplitude loadings. Int J Press Vessel Pip 1976;4:89–117.
[47] Molent L, Jones R. The influence of cyclic stress intensity threshold on fatigue life scatter. Int J Fatigue 2016;82:748–56. https://doi.org/10.1016/j.ijfatigue.2015.10.006.
[48] Caton MJ, John R, Porter WJ, Burba ME. Stress ratio effects on small fatigue crack growth in Ti-6Al-4V. Int J Fatigue 2012;38:36–45. https://doi.org/10.1016/j.ijfatigue.2011.11.004.
[49] Ali K, Peng D, Jones R, Singh RRK, Zhao XL, McMillan AJ, et al. Crack growth in a naturally corroded bridge steel. Fatigue Fract Eng Mater Struct 2017;40:1117–27. https://doi.org/10.1111/ffe.12568.
[50] Schwalbe KH. On the beauty of analytical models for fatigue crack propagation and fracture - a personal historical review. J ASTM Int 2010;7:4–73. https://doi.org/10.1520/JAI102713.
[51] Zhang X, Martina F, Ding J, Wang X, Williams SW. Fracture toughness and fatigue crack growth rate properties in wire + arc additive manufactured Ti-6Al-4V. Fatigue Fract Eng Mater Struct 2017;40:790–803. https://doi.org/10.1111/ffe.12547.
[52] Ritchie RO, Boyce BL, Campbell JP, Roder O, Thompson AW, Milligan WW. Thresholds for high-cycle fatigue in a turbine engine Ti-6Al-4V alloy. Int J Fatigue 1999;21:653–62. https://doi.org/10.1016/S0142-1123(99)00024-9.

[53] Shamir M. Fatigue crack initiation and small crack propagation in wire + arc additive manufactured Ti-6Al-4V, titnaium alloy. Coventry University; 2021.
[54] Pilkey WD, Pilkey DF. Peterson's Stress Concentration Factors. Third; 2008.
[55] Broek D, Rice JR. Chapter 3: The elastic crack-tip stress field. Elem. Eng. Fract. Mech. Third, Hague: Martinus Nijhoff; 1982. Doi: 10.1115/1.3423697.
[56] ASTM E1820: Standard Test Method for Measurement of Fracture Toughness 1 2019:1–65. Doi: 10.1520/E1820-18AE01.